

# Design of a surgical navigation system via positional tracking of fiducial markers

Darin Tsui\*, Mitsuhiro Jo\*, Bryan Nguyen\*, Farshad Ahadian\*\* and Frank E. Talke\*

\*University of California: San Diego, Center for Memory and Recording Research

9500 Gilman Drive, La Jolla, CA 92093, United States

E-mail: ftalke@ucsd.edu

\*\*University of California: San Diego Medical Center

3350 La Jolla Village Drive, San Diego, CA 92161, United States

E-mail: fahadian@health.ucsd.edu

## Abstract

Low back pain is the leading cause of non-fatal health loss and years lived with disability. Current interventional pain management therapies include epidural steroid injections and radiofrequency ablations, which can provide short-term and long-term relief. However, these therapies often utilize fluoroscopy, which exposes both the patient and medical practitioner to radiation. In this study, we explore whether an augmented reality navigation (AR) system can be interfaced with a preoperative image from magnetic resonance imaging (MRI) to reduce radiation exposure, provide a low-cost alternative to existing technologies, and improve needle position tracking. Non-invasive skin markers (ArUco) were utilized to identify the surgical field. An XYZ tracking platform with linear Kalman filtering was used to test the feasibility of marker tracking in various operating room environments. Line-of-sight obstruction was observed to affect camera tracking significantly. Future studies will address the development of a three-dimensional (3D) marker tracking system, the implementation of optimal ArUco marker materials, and ways to improve marker position accuracy.

**Keywords:** Augmented reality, Image-guided surgery, Fiducial markers, Navigation system, Marker tracking, Kalman filter, Magnetic resonance imaging

## 1. Introduction

### 1.1 Purpose

Eighty percent of all adults experience low back pain in their lifetime (Sizer, et al., 2000). In 2017 alone, 577 million individuals suffered from back pain (James, et al., 2018), with the highest prevalence in those aged 40-80 years (Manchikanti, et al., 2014).

Back pain is the leading cause of non-fatal health loss and disability globally (James, et al., 2018). Increases in obesity, physical inactivity, and an aging population have been attributed to an increase in the pervasiveness of chronic back pain (Battié, et al., 1995; Manchikanti, et al., 2014; Sizer, et al., 2000). Causes for back pain also include genetics and psychological conditions (Kovacs, et al., 2008; Croft, et al., 1995; Truchon, et al., 2008; Currie and Wang, 2005). One of the main consequences of back pain is socio-economic loss, including loss of physical and mental activity, inability to perform in occupational roles, financial burden, and relation strain (Walker, et al., 2006). Patients experiencing chronic back pain may also experience high levels of psychological distress associated with material and socio-economic losses (Walker, et al., 2006).

Advancements in medicine and technology in the last decade have increased the life expectancy of humans. It has been estimated by the United Nations that the world population of individuals aged 60 years or older will triple by 2050 (Wong, et al., 2017). The inevitably aging population increases the likelihood of non-communicable diseases such as disc degeneration, disc herniations, and outer annular tears, which all contribute to low-back pain (Battié, et al., 1995; Manchikanti, et al., 2014). It is therefore desirable to develop better and more accessible solutions for pain management

given the increasing global prevalence, high cost of surgical treatment, and debilitating effects of back pain.

## 1.2 Existing Treatments

For patients with back pain conditions that do not warrant surgery, interventional pain management therapies are available. One treatment for chronic back pain is an epidural steroid injection (ESI), which is one of the most common procedures used in pain management (Cohen, et al., 2013). In an epidural steroid injection, a medical practitioner injects corticosteroid mixture into the spine to provide temporary relief to patients with herniated discs, arthritis, and other complications (Ackerman and Ahmad, 2007). For well-selected candidates for the procedure, epidural steroid injections provide between 6 weeks and 3 months of relief. However, continuous alleviation of pain requires routine ESI procedures or further treatment, which could include surgery (Cohen, et al., 2013).

Another common procedure in pain management is radiofrequency ablation (RFA), which uses an insulated needle to administer a high frequency current to produce a temperature lesion. The presence of the lesion prevents pain signals from being sent to the brain (Rana, 2013). Radiofrequency ablation can provide pain relief lasting from 6 months to 3 years. Repeated radiofrequency ablation is also performed when symptoms return, with relief provided in 85% of patients up to 10 months (Kennedy, 2019).

A drawback to ESI, RFA, and other procedures without a surgical incision is that fluoroscopy is often utilized to determine the position of a medical instrument. This exposes both the patient and the clinicians to ionizing radiation (Kim, et al., 2016). When repeated treatments and visits are necessary such as with an epidural steroid injection, patients are exposed on a continuous basis. Furthermore, surgeons and technicians frequently use fluoroscopy more often during minimally invasive procedures, resulting in increased radiation exposure and subsequent complications (Srinivasan, et al., 2014; Mariscalco, et al., 2011).

Other techniques for determining the location of a medical instrument include the so-called loss-of-resistance (LOR) technique and ultrasonography. The loss-of-resistance technique involves identifying the spinal epidural space through a loss in physical resistance after penetrating the ligamentum flavum. A study comparing the reliability of the loss-of-resistance technique and fluoroscopy with a 20-gauge Tuohy needle showed that the loss-of-resistance technique was inferior to fluoroscopy. In particular, poor reliability was associated with patients older than 70 years and male patients (Liu, et al., 2001).

Ultrasonography was found to have superior accuracy, improved visualization of anatomy, and absence of ionizing radiation. However, it is limited due to its inability to penetrate dense tissue such as bone structures (Korbe, et al., 2015). Lumbar injections with ultrasonography were found to have poor visibility of the nerve root and neural foramen due to depth and acoustic shadowing artifacts (Narouze and Peng, 2010). Visibility was further obscured in obese patients (Korbe, et al., 2015).

It is evident that an improved and reliable navigation system without ionizing radiation is highly desirable.

## 1.3 Current State-of-the-art Technology

Image-guided surgery involves the use of intraoperative or preoperative imaging and tracking for navigational purposes. However, as more surgical instruments have become trackable, intraoperative imaging has become the standard in image-guided surgery. For intraoperative imaging in surgery, the use of augmented reality (AR) has been of significant interest (Driver and Groff, 2021). Augmented reality works by overlaying a preoperative image on live video feed or an intraoperative image, providing visualization of internal structures through overlying tissues (Lovo, et al., 2007). Existing products which utilize this technology include Philips ClarifEye and Augmedics xvision (Philips, no date; Driver and Groff, 2021; Molina, et al., 2021).

Philips ClarifEye utilizes a 3D cone-beam computed tomography (CT) to produce a 3D model of the spine. Four cameras are used to track live video images, while 8-10 non-invasive markers augment the surgical field. The video images and 3D model are overlaid to provide visual navigation, with the markers used as a reference to improve accuracy (Philips, no date). Augmedics xvision utilizes an augmented reality head-mounted display (HMD) which receives CT images from intraoperative CT scans. A registration marker is clamped onto the spinous process of the vertebrae to augment the surgical field (Molina, et al., 2021).

## 1.4 Proposed Technology

In this paper, we propose a novel 3D navigation system in order to both reduce radiation exposure and increase the speed and accuracy of needle injections performed by medical practitioners (Vávra, et al., 2017). The new navigation system involves the use of augmented reality and non-invasive skin markers coupled with an MRI scan. A preoperative MRI scan using non-invasive skin markers allows the physician to obtain a 3D model of the patient's body where surgery will be performed. This enables the physician to plan out the surgery in advance, paying special attention to the patient's individualized and unique anatomy. During the procedure, cameras will locate the skin markers on the patient's body and match them up with those in the 3D image. A physician will then be able to access the 3D model overlaid on top of the patient using an augmented reality headset. The augmented reality system will eliminate the need to periodically view an external screen by providing necessary visual information on and around the patient through the interfaced MRI image. The goal of the system will be to optimize surgical procedures by increasing the efficiency of surgical operations and reducing operation time on patients.

This paper will primarily focus on the development of the marker tracking system in two dimensions using cameras for position detection. Specifically, this paper will cover the accuracy and feasibility of tracking markers in real-time using digital filtering techniques and marker tracking libraries. Open-source markers, known as ArUco markers, will be shuttled around in 2D space at a known speed using a motorized marker platform. From here, the pixel coordinates of the markers will be exported and Kalman filtered. Finally, the measured marker positions will be compared to ground-truth marker platform distances.

## 2. Nomenclature Table

Important symbols are defined as shown below.

$x_k$	position in the x direction
$y_k$	position in the y direction
$\dot{x}_k$	velocity in the x direction
$\dot{y}_k$	velocity in the y direction
$\ddot{x}_k$	acceleration in the x direction
$\ddot{y}_k$	acceleration in the y direction
$F$	state transition matrix
$H$	observation matrix

## 3. Development Process

### 3.1 XYZ Platform

In order to simulate marker tracking, a ground truth testing platform was built as shown in Fig. 1. An XYZ platform was chosen to simulate marker movements of patients during a procedure. Figure 1 shows the computer-aided design of the system, and Fig. 2 shows the constructed XYZ platform.

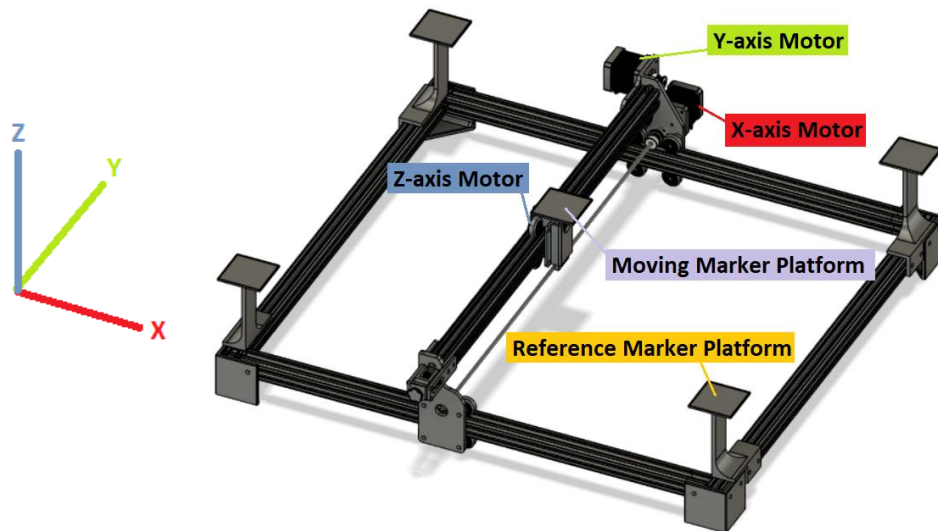


Fig. 1 Computer-aided design model of the XYZ platform. The XYZ platform comes with three stepper motors to move the marker platform in the X, Y, and Z directions. The reference marker platforms are fixed.

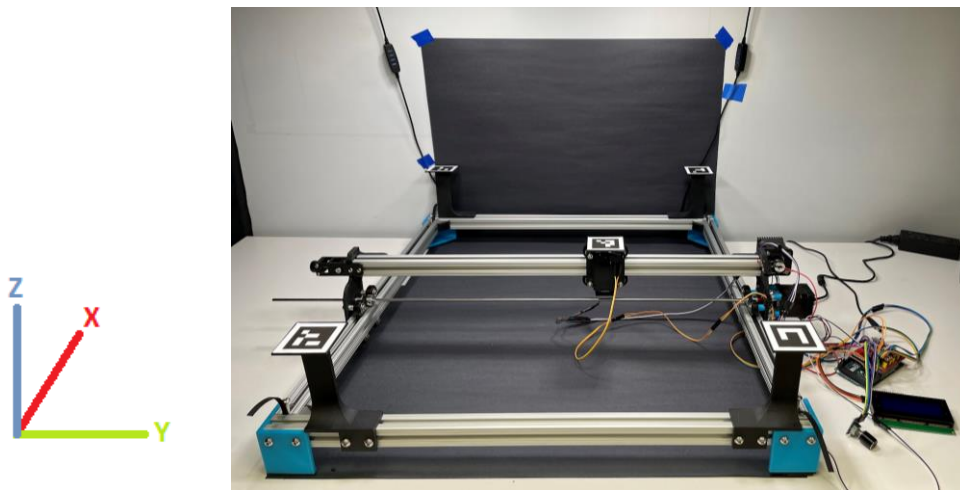


Fig. 2 Physical model of the XYZ platform. The moving marker is able to move in the X, Y, and Z directions. The X, Y, and Z motors are controlled via Arduino. The reference markers are located at the corners of the XYZ platform and are fixed.

The movement of the platform is controlled by the X, Y, and Z axis stepper motors, which move the marker platform around. From the perspective of Fig 2., the X axis is defined as the marker moving towards and away from the page, and the Y axis is defined as the marker moving left and right. The Z axis is defined as the marker moving up and down. The reference marker platforms on the edges of the platform are stationary and are used as fixed positions for the marker tracking software to reference.

### 3.2 Marker Tracking Implementation

“ArUco” markers are open-source fiducial markers dedicated to positional tracking in real time. Figure 3 shows the anatomy of a typical ArUco marker. The bit grid inside the inner black border of the ArUco marker is used to facilitate marker identification. The outer white margin of the marker is used to separate the marker itself from the background for optimal detection (*OpenCV*, no date). The ArUco code can be thought of as a two-dimensional bar code.

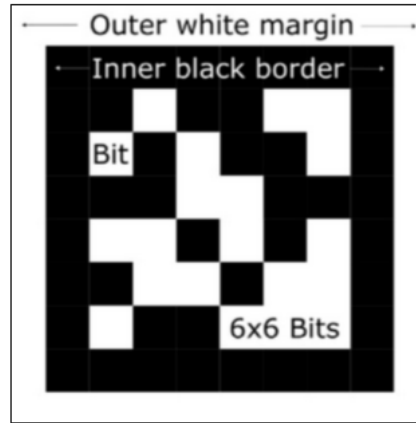


Fig. 3 Details of a typical ArUco code marker. The white bits of information inside the inner black border serve to track the marker ID as the marker moves in real time. The outer white margin is used to provide a visual barrier between the background and the actual marker itself.

The ArUco marker library was utilized to facilitate marker tracking (Garrido-Jurado, et al., 2014). OpenCV was used to interface the markers within Python (*OpenCV*, no date). This was done by tracking the center pixel coordinates of the markers as they move through space. Using this, the relative position of the moving marker with respect to each of the reference markers can be determined. Since the reference markers are fixed, a world frame of reference is created for analysis from the camera’s frame of reference. Table 1 displays the default parameters used in testing. Pixel density refers to the number of bits encoding the marker identification information. For example, in Fig. 3, the pixel density is 6x6 pixels.

Table 1 Default parameters used in marker experiments.

Parameters	Settings
Marker platform speed	10 mm/s
Pixel density	4x4 pixels
Pixel size	4 cm
White border width	1 bit
Camera resolution	1080p
Frames per second	60 fps

In this implementation, video recordings of markers moving on the XYZ platform were taken using a smartphone camera. The camera was calibrated according to ArUco documentation (*OpenCV*, no date). Videos were processed in Python using OpenCV to output the pixel coordinates of the markers relative to the reference markers.

### 3.3 Kalman Filtering Implementation

To improve marker tracking, Kalman filtering was implemented in Python as part of post-processing. Kalman filtering is a widely used sensor and data fusion algorithm for dynamic applications. The basic Kalman filter is discrete, recursive, and derives an estimated state of a linear system in real-time. General applications for Kalman filtering include vehicle navigation, radar sensors, and computer vision measurements. For more complex non-linear applications such as

satellite navigation, the extended Kalman filter (EKF) is used (Alsadik, 2019).

Other non-linear Kalman filters used for localization, target tracking, and navigation include the unscented Kalman filter, ensemble Kalman filter, and constrained Kalman filter (Ting Goh, et al., 2018). Further applications include the implementation of a linear Kalman filter in object pose tracking with ArUco markers. In applications of marker tracking, linear Kalman filtering was found to reduce tracking noise and was able to estimate marker position during temporary instances when the camera was unable to detect markers due to obstructing objects (Kam, et al., 2018).

In 2D Kalman filtering, the kinematic state equations describing the marker tracking system can be written. The rows in Eq. (1) correspond with the variables  $x_k$ ,  $y_k$ ,  $\dot{x}_k$ , and  $\dot{y}_k$ , respectively.

$$\mathbf{x}_k = \begin{bmatrix} x_k + \dot{x}_{k-1}\Delta t + \frac{1}{2}\ddot{x}_{k-1}\Delta t^2 \\ y_k + \dot{y}_{k-1}\Delta t + \frac{1}{2}\ddot{y}_{k-1}\Delta t^2 \\ \dot{x}_{k-1} + \ddot{x}_{k-1}\Delta t \\ \dot{y}_{k-1} + \ddot{y}_{k-1}\Delta t \end{bmatrix} \quad (1)$$

In the experimental system, acceleration is assumed to be negligible since the motors are assumed to be moving at constant velocity. Thus, the state transition matrix  $F$  can be written.

$$F = \begin{bmatrix} 1 & 0 & \Delta t & 0 \\ 0 & 1 & 0 & \Delta t \\ 0 & 0 & 1 & 0 \\ 0 & 0 & 0 & 1 \end{bmatrix} \quad (2)$$

The position of the moving marker in the X and Y directions in real-time are the required inputs. Therefore, the observation matrix  $H$  can be written.

$$H = \begin{bmatrix} 1 & 0 & 0 & 0 \\ 0 & 1 & 0 & 0 \end{bmatrix} \quad (3)$$

This Kalman filtering implementation was applied to the positional information of the moving marker and implemented using the Pykalman library in Python (*pykalman*, no date).

## 4. Results

### 4.1 XYZ Platform Performance

The positional errors of the XYZ platform were calculated through reset and incremental testing. In reset tests, the moving marker platform was moved 10 mm to 300 mm in increments of 10 mm spacings in the X and Y directions. In the Z direction, the moving marker platform was moved from 3 mm to 45 mm in increments of 3 mm spacings. After each movement, the error was recorded, and the error was “reset” back to zero. After each trial, the error was recorded, and the markers were reset to their original position. In incremental tests, the moving marker was moved in 10 mm increments in the X and Y direction until it travelled 300 mm. In the Z direction, the moving marker was moved in 3 mm increments until it reached 45 mm. Table 2 shows the mean error results in the X, Y, and Z directions in the reset test. Table 3 shows the mean error results in the incremental test.

Table 2 Directional mean error in the reset tests.

Direction	Mean Error
X	$-0.11 \pm 0.07$ mm
Y	$-0.06 \pm 0.09$ mm
Z	$0.02 \pm 0.11$ mm

Table 3 Directional mean error in the incremental tests.

Direction	Mean Error
X	$-0.003 \pm 0.072$ mm
Y	$-0.005 \pm 0.080$ mm
Z	$0.005 \pm 0.007$ mm

From Table 2, both the X and Y directions appear to underestimate distance. However, from Table 3, there does not appear to be significant underestimating of errors. This suggests that the marker platform performs consistently independently of its location on the X and Y axis.

Speed tests were also analyzed in the XYZ platform. In the X and Y direction, the marker platform was tested at 10, 15, and 20 mm/s at distances of 120, 240, and 480 mm, respectively. In the Z direction, the marker platform was tested at 10, 15, and 20 cycles per minute, where the maximum displacement was between one to three centimeters. This was done in order to simulate breathing rates and chest expansion/compression motion. Videos were taken from a top-down view for the X and Y directions, and from a front-back view for the Z direction. These videos were analyzed frame by frame to determine the start and stop times of experimental runs. Table 4 shows the marker platform speeds measured in the X and Y directions. Table 5 shows the marker platform speeds in the Z direction. The estimated distance errors propagated into the experimental speed errors, with the time frame of 1 frame (1/60 seconds).

Table 4 Experimental platform speeds in the X and Y directions.

Direction	Distance Travelled (mm)	Theoretical Speed (mm/s)	Experimental Speed (mm/s)
X	120	10	$9.89 \pm 0.02$
X	120	15	$14.88 \pm 0.03$
X	120	20	$19.73 \pm 0.04$
Y	120	10	$9.88 \pm 0.02$
Y	120	15	$14.92 \pm 0.03$
Y	120	20	$19.77 \pm 0.04$
X	240	10	$9.88 \pm 0.01$
X	240	15	$14.88 \pm 0.01$
X	240	20	$19.73 \pm 0.02$
Y	240	10	$9.87 \pm 0.01$
Y	240	15	$14.90 \pm 0.02$
Y	240	20	$19.74 \pm 0.02$
X	480	10	$9.88 \pm 0.01$
X	480	15	$14.87 \pm 0.01$
X	480	20	$19.73 \pm 0.01$
Y	480	10	$9.87 \pm 0.01$
Y	480	15	$14.89 \pm 0.01$
Y	480	20	$19.72 \pm 0.01$

Table 5 Experimental platform speeds in the Z direction.

Direction	Displacement (cm)	Cycles per minute (cycles/min)	Experimental Speed (mm/s)
Z	1	10	$9.98 \pm 0.02$
Z	1	15	$14.94 \pm 0.02$
Z	1	20	$19.97 \pm 0.02$
Z	3	10	$9.95 \pm 0.02$
Z	3	15	$14.92 \pm 0.02$
Z	3	20	$19.87 \pm 0.02$

From Tables 4 and 5, it is clear that the platform slightly underperformed the intended speeds in all directions. However, through these marker speed and distance tests, the error associated with the marker platform can be effectively quantified. These experimental speed tests will be used as a ground truth when conducting marker tracking experiments.

## 4.2 Marker Tracking Performance

During marker tracking tests, coordinate data of the moving marker was exported into MATLAB for analysis. Kalman filtering was then applied on the coordinate data during post-processing. An example of the marker moving at 10 mm/s is displayed in Fig. 4. Here, each color corresponds to one movement of the XYZ platform. The average position of three trials was used in plotting.

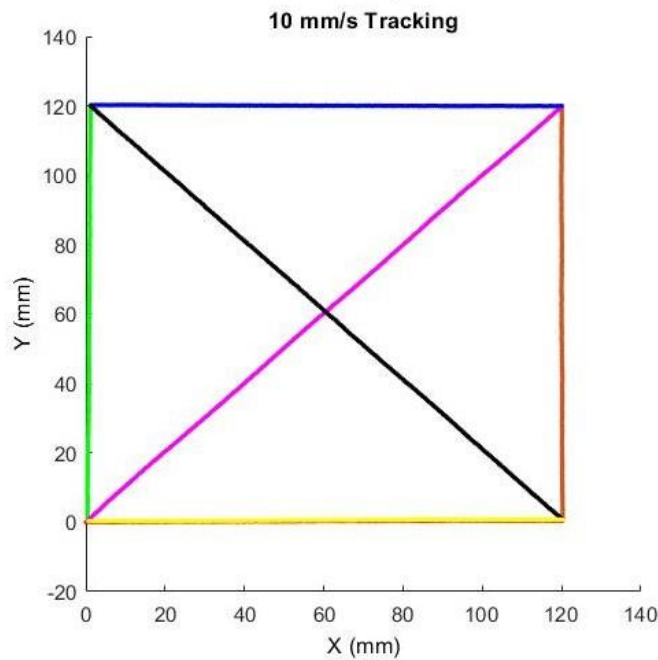


Fig. 4 Plotted coordinates of the marker moving on the testing platform at 10 mm/s. The average position of three trials was used in plotting. Each color corresponds to one movement of the XYZ platform.

The position of the moving marker was compared against the ideal position of the marker associated with the velocity of the motor determined in reset tests. The error of the moving marker was plotted as the marker moved through space. Figure 5 displays the error heatmap of the marker moving at 10 mm/s. The average error of three trials was used. Table 6 shows the error results of the moving marker at 10, 15, and 20 mm/s for three trials each.



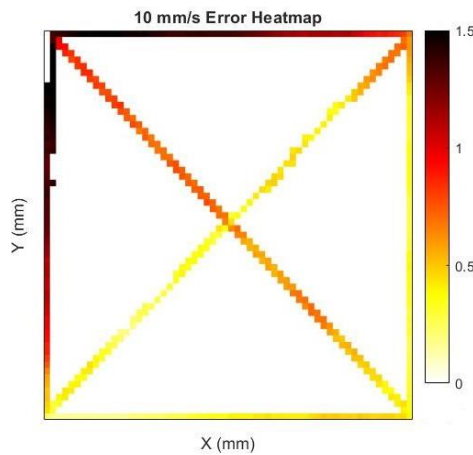


Fig. 5 Error heatmap of the marker moving on the testing platform at 10 mm/s. The error was calculated by comparing the ideal position of the marker, in accordance with experimental motor speeds, to the position tracked by marker tracking software. The average error of three trials was used to plot the heatmap.

Table 6 Moving marker error results at different speeds

Speed (mm/s)	Trial 1 (mm)	Trial 2 (mm)	Trial 3 (mm)
10	$1.0 \pm 0.7$	$0.8 \pm 0.5$	$0.7 \pm 0.4$
15	$1.0 \pm 0.3$	$1.1 \pm 0.5$	$0.9 \pm 0.5$
20	$0.7 \pm 0.3$	$0.8 \pm 0.3$	$0.7 \pm 0.2$

From Fig. 5, we observe that the largest error occurs near the top left of the platform. This is due to the position of the tracking camera relative to the platform being closer to the front of the platform. Table 6 shows that the majority of trials run at 10, 15, and 20 mm/s recorded average errors of about 1 mm. Factors that could affect tracking quality were examined, including the moving marker speed, number of reference markers used, line-of-sight obstruction, size of the white marker border, marker contrast between the inner black border and outer white margin, and marker warping. We concluded that the factors generating the largest errors included the following: line-of-sight obstruction, camera distance, and the size of the white marker border. Respective error figures are provided in the Appendix.

## 5. Discussion

The marker tracking system development is very promising. The maximum error of the moving markers was approximately 1.5 mm when testing different marker platform speeds. For this situation, the average error across all three trials was less than 1 mm. Aside from the marker platform itself, tracking the moving marker was proven to be cost effective, since it only requires a camera.

Currently, we are developing a 3D marker tracking system, but this comes with its own challenges. For example, factors such as potential stretching or rotation of markers in space during the tracking will need to be accounted for. After developing the tracking system, fiducial markers must be interfaced with a preoperative MRI scan through augmented reality. In addition, attention needs to be given to marker deformation on the skin to ensure the feasibility of using a 3D map based on an MRI scan. Potential solutions for offsetting the scale of deformation would be to utilize multiple reference markers on the patient, as well as accounting for changes in marker position using tracking software calibration. Testing of such software implementations could begin on artificial tissue samples to get an idea of the deformations that may occur during real-life studies.

Improvements to the quality of positional readings from the marker should be explored as well. On the hardware side, experimenting with better quality cameras will be needed for improving the accuracy of the system. Using a multitude of cameras during tracking could also prove useful in detecting outlier readings. In terms of software, better digital filtering techniques could be explored as well. For example, the implementation of a weighted mean average filter could stabilize readings over a set sliding time window.

An optimal marker adhesive also must be narrowed down through various material tests, such as testing for creep, peel, and durability. The material must also pass cytotoxicity, biocompatibility, and irritation tests to be compatible with human experiments. Additionally, such a marker material would also have to be detectable and trackable by camera software, regardless of potential wear and tear that may occur between the time of an MRI scan and the time of an operation.

In addition to mechanical optimizations, anesthesiologists and physicians will need to be consulted to direct the design and setup of the marker tracking system towards effective usage in the operating room. Special attention will need to be made towards catering the system to the ergonomics of the physicians. While the augmented reality tracking system has a plethora of future work, significant research and development towards the system has demonstrated the potential feasibility of fielding a marker tracking system in the operating room.

## **6. Conclusion**

In this study, we explore the possibility of creating an augmented reality system that can be interfaced with MRI to aid in positional tracking of surgical instruments with respect to operation areas of interest. An XYZ platform was developed in order to conduct ground-truth testing on marker tracking software in 2D. ArUco markers in conjunction with linear Kalman filtering were used in order to track the position of moving markers across the platform.

Future work on this project will address the development of a 3D marker tracking system, as well as further development towards finding optimal marker adhesive materials and integration with preoperative MRI scans. The ultimate goal of the surgical system is to reduce radiation exposure while simultaneously providing a low-cost alternative to existing surgical-assisting technologies.

## **Acknowledgements**

This work was supported in part by a grant from the UCSD General Campus Research Senate #2019201 and the UCSD ACTRI-IEM GEM Grant #1020487.

## **Appendix**

This appendix describes the various other tests conducted towards the tracking of markers. Figure A1 describes the error heatmaps of the marker moving on the testing platform at 10, 15, and 20 mm/s for each individual marker trial. These heatmaps serve as complements to Table 6, which describes the average error for all trials for each of the marker speeds.

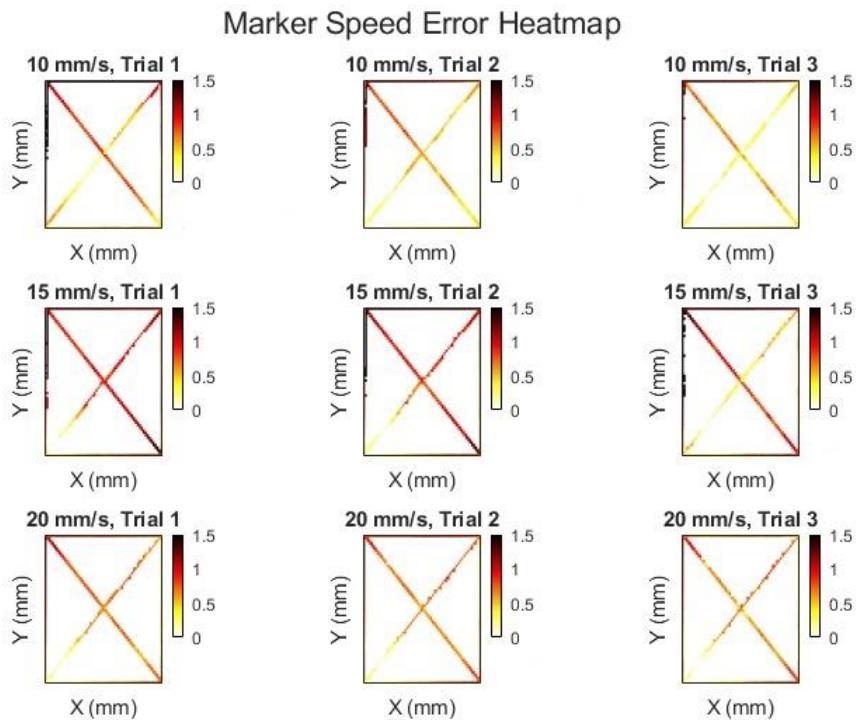


Fig. A1 Plotted coordinates of the marker moving on the testing platform at 10, 15, and 20 mm/s. Three trials were performed and plotted. Each color corresponds to one movement of the XYZ platform.

To test for line-of-sight obstruction, the moving marker was partially obstructed using a black strip that covered sections of the marker. The black strip was moved across the marker from top to bottom, left to right, and across the marker’s diagonals in order to cover significant amounts of area. The thickness of the black strip varied between 0-1.5 bits in thickness. Table A1 displays the results found in these tests. These tests were measured as the percentage of time the marker was detected during the trials.

Table A1    Detection percentage in line-of-sight obstruction tests

Obstruction thickness	Detection Percentage
0 bits	100%
0.5 bits	14.17%
1 bit	0%
1.5 bits	0%

Here, it was shown that even slight obstructions across the marker resulted in significant losses in detection percentage. Future optimizations of the marker tracking system will need to take optical obstruction into account as a potential limiter to surgical tracking.

Another parameter tested for marker tracking accuracy was the distance between the center of the marker tracking platform to the external camera setup. Tests were performed when the camera was 50, 60, and 70 cm away from the platform. Three trials were performed in determining the average error associated with the marker tracking. From these experiments, it was found that the average error grew as the camera distance increased. Table A2 shows the average error results for the varied camera distances over the three trials performed.

Table A2 Average error results for varied camera distances

Distance (cm)	Trial 1 (mm)	Trial 2 (mm)	Trial 3 (mm)
50	$0.8 \pm 0.5$	$0.7 \pm 0.4$	$0.7 \pm 0.3$
60	$1.0 \pm 0.4$	$1.0 \pm 0.4$	$0.8 \pm 0.3$
70	$1.2 \pm 0.5$	$1.4 \pm 0.6$	$1.3 \pm 0.5$

Finally, the size of the outer white margin was varied to determine its effect on marker tracking. The white margin thickness was varied between 0-2 bits in the three trials performed, and the errors were averaged across each of the individual trials. It was found that using an outer white margin of 0 and 0.5 bits resulted in the moving marker barely being detected at all. Table A3 displays the findings for 0 and 0.5 bits. Due to the poor performance of the marker, these trial values are expressed in the percentage of time the marker was detected, rather than quantifying marker performance in terms of accuracy.

Table A3 Detection percentage in white margin thickness tests

Thickness	Trial 1	Trial 2	Trial 3
0 bits	0% detected	0% detected	0% detected
0.5 bits	3.14% detected	3.63% detected	3.56% detected

For white margin thickness of 1 bit and above, the error was able to be quantified in terms of average error across each of the individual trials. Table A4 displays the findings for these thicknesses.

Table A4 Average error results for varied white margin thicknesses

Thickness	Trial 1 (mm)	Trial 2 (mm)	Trial 3 (mm)
1 bit	$1.2 \pm 0.6$	$1.0 \pm 0.4$	$0.9 \pm 0.4$
1.5 bits	$1.0 \pm 0.4$	$1.0 \pm 0.4$	$0.9 \pm 0.4$
2 bits	$1.0 \pm 0.4$	$1.0 \pm 0.4$	$0.9 \pm 0.4$

The error results when varying the white margin thicknesses at or above 1 bit tended to be stable. However, for tests conducted with white margins of 0- and 0.5-bit thickness, the markers were unable to be properly detected. This set of tests affirms the importance of the white margin in terms of tracking markers in space.

## References

- Ackerman, W.E. and Ahmad, M., 'The efficacy of lumbar epidural steroid injections in patients with lumbar disc herniations', *Anesthesia and Analgesia*, Vol.104, No.5 (2007), pp.1217–1222.
- Alsadik, B., 'Chapter 10 - Kalman Filter', in B. Alsadik (ed.) *Adjustment Models in 3D Geomatics and Computational Geophysics*. Elsevier (Computational Geophysics) (2019), pp.299–326.
- Battié, M.C. *et al.*, '1995 Volvo Award in clinical sciences. Determinants of lumbar disc degeneration. A study relating lifetime exposures and magnetic resonance imaging findings in identical twins', *Spine*, Vol.20, No.24 (1995), pp.2601–2612.
- Philips ClarifEye Augmented Reality Surgical Navigation* (no date), available from <https://www.philips.com/a-w/about/news/media-library/20210202-clarifeye-augmented-reality-surgical-navigation.html>, (accessed on 7 December, 2021).
- Cohen, S.P. *et al.*, 'Epidural steroids: a comprehensive, evidence-based review', *Regional Anesthesia and Pain Medicine*, Vol.38, No.3 (2013), pp.175–200.
- Croft, P.R. *et al.*, 'Psychologic distress and low back pain. Evidence from a prospective study in the general population', *Spine*, Vol.20, No.24 (1995), pp.2731–2737.

- Currie, S.R. and Wang, J., 'More data on major depression as an antecedent risk factor for first onset of chronic back pain', *Psychological Medicine*, Vol.35, No.9 (2005), pp.1275–1282.
- Driver, J. and Groff, M.W., 'Editorial. Navigation in spine surgery: an innovation here to stay', *Journal of Neurosurgery: Spine*, Vol.36, No.3 (2021), pp.347–349.
- Garrido-Jurado, S. *et al.*, 'Automatic generation and detection of highly reliable fiducial markers under occlusion', *Pattern Recognition*, Vol.47, No.6 (2014), pp.2280–2292.
- James, S.L. *et al.* 'Global, regional, and national incidence, prevalence, and years lived with disability for 354 diseases and injuries for 195 countries and territories, 1990–2017: a systematic analysis for the Global Burden of Disease Study 2017', *The Lancet*, Vol.392, No.10159 (2018), pp.1789–1858.
- Kam, H.C., Yu, Y.K. and Wong, K.H., 'An Improvement on ArUco Marker for Pose Tracking Using Kalman Filter', in *2018 19th IEEE/ACIS International Conference on Software Engineering, Artificial Intelligence, Networking and Parallel/Distributed Computing (SNPD). 2018 19th IEEE/ACIS International Conference on Software Engineering, Artificial Intelligence, Networking and Parallel/Distributed Computing (SNPD)* (2018), pp.65–69.
- Kennedy, D., *Radiofrequency Ablation (RFA) for Facet and Sacroiliac Joint Pain, Spine-health* (no date), available from <<https://www.spine-health.com/treatment/injections/radiofrequency-ablation-rfa-facet-and-sacroiliac-joint-pain>>, (accessed on 26 November, 2021).
- Kim, S. *et al.*, 'Factors Affecting Radiation Exposure during Lumbar Epidural Steroid Injection: A Prospective Study in 759 Patients', *Korean Journal of Radiology*, Vol.17, No.3 (2016), pp. 405–412.
- Korbe, S. *et al.*, 'Ultrasound-guided interventional procedures for chronic pain management', *Pain Management*, Vol.5, No.6 (2015), pp.465–482.
- Kovacs, F. *et al.*, 'The Influence of Psychological Factors on Low Back Pain-Related Disability in Community Dwelling Older Persons', *Pain Medicine*, Vol.9 No.7 (2008), pp.871–880.
- Liu, S.S. *et al.*, 'Prospective experience with a 20-gauge Tuohy needle for lumbar epidural steroid injections: Is confirmation with fluoroscopy necessary?', *Regional Anesthesia and Pain Medicine*, Vol.26, No.2 (2001), pp.143–146.
- Lovo, E.E. *et al.*, 'A novel, inexpensive method of image coregistration for applications in image-guided surgery using augmented reality', *Neurosurgery*, Vol.60, No.4 (Suppl 2) (2007), pp.366–371; discussion 371–372.
- Manchikanti, L. *et al.*, 'Epidemiology of Low Back Pain in Adults', *Neuromodulation: Technology at the Neural Interface*, Vol.17 (2014), pp.3–10.
- Mariscalco, M.W. *et al.*, 'Radiation exposure to the surgeon during open lumbar microdiscectomy and minimally invasive microdiscectomy: a prospective, controlled trial', *Spine*, Vol.36, No.3 (2011), pp.255–260.
- Molina, C.A. *et al.*, 'Clinical Accuracy, Technical Precision, and Workflow of the First in Human Use of an Augmented-Reality Head-Mounted Display Stereotactic Navigation System for Spine Surgery', *Operative Neurosurgery*, Vol.20, No.3 (2021), pp.300–309.
- Narouze, S. and Peng, P.W.H., 'Ultrasound-guided interventional procedures in pain medicine: a review of anatomy, sonoanatomy, and procedures. Part II: axial structures', *Regional Anesthesia and Pain Medicine*, Vol.35, No.4 (2010), pp.386–396.
- OpenCV: *ArUco marker detection (aruco module)* (no date), available from <[https://docs.opencv.org/4.x/d9/d6d/tutorial\\_table\\_of\\_content\\_aruco.html](https://docs.opencv.org/4.x/d9/d6d/tutorial_table_of_content_aruco.html)>, (accessed on 16 February 2022).
- pykalman — *pykalman 0.9.2 documentation* (2012), available from <<https://pykalman.github.io/>>, (accessed on 3 July 2022).
- Rana, M.V., 'Radiofrequency: Conventional and Pulsed', in T.R. Deer et al. (eds) *Comprehensive Treatment of Chronic Pain by Medical, Interventional, and Integrative Approaches*. New York, NY: Springer New York (2013), pp.285–296.

- Sizer, P.S., Matthijs, O. and Phelps, V., 'Influence of age on the development of pathology', *Current Review of Pain*, Vol.4, No.5 (2000), pp.362–373.
- Srinivasan, D. *et al.*, 'Radiation safety and spine surgery: systematic review of exposure limits and methods to minimize radiation exposure', *World Neurosurgery*, Vol.82, No.6 (2014), pp.1337–1343.
- Ting Goh, S., (Reza) Zekavat, S.A. and Abdelkhalik, O., 'An Introduction to Kalman Filtering Implementation for Localization and Tracking Applications', in *Handbook of Position Location*. John Wiley & Sons, Ltd (2018), pp.143–195.
- Truchon, M. *et al.*, 'Low-back-pain related disability: An integration of psychological risk factors into the stress process model', *Pain*, Vol.137, No.3 (2008), pp.564–573.
- Vávra, P. *et al.*, 'Recent Development of Augmented Reality in Surgery: A Review', *Journal of Healthcare Engineering* (2017), pp.1–9.
- Walker, J., Sofaer, B. and Holloway, I., 'The experience of chronic back pain: Accounts of loss in those seeking help from pain clinics', *European Journal of Pain*, Vol.10, No.3 (2006), pp.199–199.
- Wong, A.Y., Karppinen, J. and Samartzis, D., 'Low back pain in older adults: risk factors, management options and future directions', *Scoliosis and Spinal Disorders*, Vol.12, No.14 (2017).